

# **Formation Sequence of Fe–Al Intermetallic Phases at Interface between Solid Fe and Liquid Zn–6Al–3Mg Alloy**

Hiroki Yokoi<sup>1</sup>, Naoki Takata<sup>1\*</sup>, Asuka Suzuki<sup>1</sup>, Makoto Kobashi<sup>1</sup>

<sup>1</sup>Department of Materials Process Engineering, Graduate School of Engineering,  
Nagoya University, Furo-cho, Chikusa-ku, Nagoya, 464-8603 Japan

\*Corresponding author,

E-mail address: takata.naoki@material.nagoya-u.ac.jp (N. Takata)

**Keywords:** galvanized steels; Zn–Al–Mg alloy coating; interfacial reaction;  
thermodynamic calculation; Fe<sub>2</sub>Al<sub>5</sub> phase

## Abstract

In the present study, we characterized the Fe–Al intermetallic phases formed in interstitial-free (IF) steel hot-dipped in a Zn–6Al–3Mg (wt.%) alloy melt at different temperatures (400, 460 and 500°C) and dipping times (from 2 to 3600 s). Chemical composition analyses indicated Fe dissolution into the Zn alloy melt even after 2 s of dipping. Microstructural characterization revealed the initial formation of a continuous  $\theta$ -Fe<sub>4</sub>Al<sub>13</sub> phase layer, followed by the local growth of  $\eta$ -Fe<sub>2</sub>Al<sub>5</sub> phase toward both steel and Zn alloy melt sides during the hot-dipping process. After long-term hot-dipping, further growth of the  $\eta$  phase was accompanied by significant dissolution of Fe into the Zn alloy melt, resulting in the loss of thickness of the IF steel sheets. Altogether, we rationalized the formation mechanism of Fe–Al intermetallic phases and their associated growth at the interface between solid Fe and liquid Zn alloy in terms of a Zn–Al–Mg–Fe quaternary phase diagram, calculated according to thermodynamic database available in the literature.

## 1. Introduction

Hot-dip zinc (Zn) and its alloy coating on steels (galvanized steels) are extensively produced for architectural and automobile applications because of their low cost and sufficient corrosion resistance under atmospheric environments [1, 2]. In particular, Zn–Al–Mg ternary alloy coatings exhibit superior corrosion resistance [3–5]. The associated hot-dip galvanizing technologies are being applied to building steel parts [6]. However, there is a concern over the hot-dip Zn–Al–Mg alloy galvanizing process to steel parts, that is, the sufficient adhesiveness of the Zn alloy coating layer on the steel parts. It is generally known that Al-rich Fe–Al intermetallic phase layers consisting of  $\theta$ -Fe<sub>4</sub>Al<sub>13</sub> and  $\eta$ -Fe<sub>2</sub>Al<sub>5</sub> phases [7] are often formed at the interface between the Zn–Al–Mg alloy coating and the steel parts [8–12]. These Al-rich Fe–Al intermetallic phases show brittle properties [13], requiring controlled formation of the Fe–Al intermetallic phases in the Zn–Al–Mg alloy coating on steel parts. It is, therefore, necessary to understand the interfacial reaction between the steel parts (solid  $\alpha$ -Fe, also known as ferrite) and the Zn alloy melt (liquid Zn alloy) during the hot-dip galvanizing process [1].

It has been demonstrated in previous studies [8–12] that alloy contents and additional trace elements in the Zn–Al–Mg alloy melts significantly influence the formation and growth of the Fe–Al intermetallic phases on the steel sheets hot-dipped in Zn alloy melts. It has also been reported that a coarse Fe–Al intermetallic phase ( $\eta$ -Fe<sub>2</sub>Al<sub>5</sub>) can be formed on steels hot-dipped in Zn alloy melts with a high Al content [8], whereas the Mg content in the Zn–Al–Mg ternary alloy melt would inhibit the formation of the Fe–Al intermetallic phase layer on the steels [12]. In contrast, Fe–Al intermetallic phases were scarcely observed in commercial hot-dip Zn–Al–Mg alloy coated steels [14], which might be related to the short-term dipping time (of a few seconds) employed in the industrial hot-dip galvanizing process [1]. Kinetics studies on the growth of Fe–Al intermetallic phase layers in the hot-dip galvanizing process using Zn–Al–Mg alloy melts are seldom reported. Therefore, the formation sequence of Fe–Al

intermetallic phases and their related growth process at the interface between solid Fe (steel) and liquid Zn alloys remains unclear.

Herein, we focus on the Zn–6Al–3Mg (wt.%) alloy coating, given its commercial relevance. We characterized the Fe–Al intermetallic phase layer formed on the interstitial-free (IF) steel hot-dipped in the Zn–6Al–3Mg alloy melt at various temperatures (400, 460, and 500°C) and different dipping periods (ranging from 2 to 3,600 s). The results, in conjunction with the calculated Zn–Al–Mg–Fe quaternary phase diagram, were utilized to discuss the formation sequence of Fe–Al intermetallic phases and their associated growth during the hot-dip galvanizing process.

## 2. Experimental Procedure

IF steel sheets were used as a model system for pure iron, with a ferrite ( $\alpha$ -Fe) single-phase microstructure. The detailed chemical composition of the studied IF steel is shown in [Table 1](#). The steel sheet was hot-rolled and then cold-rolled to about 1.2 mm in thickness. Hot-dipping experiments were carried out using a hot-dip process simulator [\[15, 16\]](#). Before the hot-dipping experiment, the steel sheets were mechanically polished and finished with buffing compounds. The alloy sheets, with approximate dimensions of  $210 \times 105 \times 1.2$  mm, were heated to 800°C for 60 s and then cooled down to Zn alloy bath temperature (400, 460, and 500°C) under  $N_2/H_2$  atmosphere (50 : 50 in %vol.). The sheets were then hot-dipped in a molten Zn–6Al–3Mg (wt.%) alloy (Zn–12.8Al–7.1Mg, at%) bath at different temperatures (400, 460, and 500°C) and dipping times (from 2 to 3600 s), followed by rapid cooling via a gas wiping system. The composition of the used Zn alloy plotted on the calculated liquidus projection of the Zn–Al–Mg ternary system based on previously published thermodynamic database [\[17\]](#) is illustrated in [Fig. 1](#). The liquidus projection provides an indication of the solidification path. In the studied Zn–6Al–3Mg (wt.%) alloy, the  $\alpha$ -Al (fcc) phase initially solidifies, followed by a three-phase eutectic reaction of  $\alpha$ -Al (fcc), Zn (hcp) and  $Zn_{11}Mg_2$  [\[18\]](#) phases, and then  $Zn_2Mg$  phase [\[19\]](#) finally forms. The liquidus projection

provides a prediction of the solidification microstructure in the studied Zn alloy coating on the steel sheets. Heat profiles of the sheets during the hot-dipping process were measured using K-type thermocouples welded on the top portion of the sheet surface. The representative thermal profiles of the IF steel sheets during the hot-dipping experiment (dipping for 600 s) are presented in Fig. 2. The temperature deviation of the samples during dipping in the Zn alloy melt was within 2°C. The sample cooling rate after hot-dipping was approximately 10°C/s.

The microstructures of the prepared samples were observed using a scanning electron microscope (SEM) operating at 20 kV. The observed sample surfaces were mechanically polished and finished using colloidal silica. Low-magnification SEM images were used to measure the thickness of the alloy sheets. For high-magnification SEM observation, the sample surface was ion-polished with a cross section polisher operated at 6 kV. The chemical compositions were analyzed using energy-dispersive X-ray spectroscopy (EDS), operated at 15 kV. The constituent phases of the intermetallic phase layer were identified using electron back-scatter diffraction (EBSD) analysis. The constituent phases of the hot-dipped samples were identified using X-ray diffraction (XRD) equipped with a Cu target tube with  $\lambda_{K\alpha} = 0.154$  nm. In this study, XRD was performed on cross-sectional samples of the steel sheets dipped in the Zn alloy melt.

### 3. Results

#### 3.1. Thickness Loss of the Steel Sheets during Dipping

Figure 3 shows the back-scattered electron images (BEIs) of the cross section of the IF steel sheets hot-dipped in the Zn–6Al–3Mg alloy melt at different temperatures, ranging from 400 to 500°C, for 2, 600, and 3600 s. In these images, bright, dark and intermediate-contrast areas correspond to IF steel sheets, resins (for mounting the samples), and Zn alloy coating layers, respectively. In the early stage of dipping (2 s), all steel sheets dipped in the Zn alloy melt exhibited a coating thickness (corresponding to bright regions) of approximately 20  $\mu\text{m}$  (Figs. 3(a), 3(d), and 3(g)). In the samples hot-dipped for 600 s (Figs. 3(b), 3(e), and

3(h)), the higher the temperature, the thicker the Zn alloy coating formed on the IF steel sheet. It is evident that a large Zn coating with a mean thickness of more than 300  $\mu\text{m}$  forms on the steel sheet hot-dipped at 500°C (Fig. 3(b)), which corresponds to the presence of coarse intermetallic phases in the Zn alloy melt. This trend appears more pronounced at higher temperature for longer dipping time (Figs. 3(c) and 3(f)), whereas the anomaly large intermetallic phases were observed in the sample hot-dipped at 460°C for 3,600 s (Fig. 3(c)). It should be noted that the thickness of the steel sheet (without the Zn alloy coating layer) clearly decreases after dipping in the Zn melt for 3,600 s (Figs. 3(c) and 3(f)), indicating a significant dissolution of Fe into the Zn alloy melt.

Figure 4 presents the effect of temperature on the thickness change of the steel sheet samples dipped in the Zn–6Al–3Mg alloy melt. Differences from the initial thickness before dipping (approximately 1.2 mm) are plotted on the vertical axis of Fig. 4. Note that the thicknesses of the steel sheets after dipping were measured using the SEM images (as shown in Fig. 3). The sheet thickness barely changes at 400°C, even after 3600 s of dipping, whereas the thickness loss was clearly observed in the samples hot-dipped at higher temperatures. At 460°C, the sheet thickness remained unchanged until 600 s and then decreased after 3,600 s. At 500°C, the thickness slightly decreased until 60 s and then significantly decreased to two-thirds the initial thickness after 3,600 s, indicating significant dissolution of the steel sheet into the Zn alloy melt during dipping. The Fe dissolution into the Zn melt was previously observed in steel sheets hot-dipped in pure Zn and Zn–Al alloy melts as well [20, 21].

In order to examine the Fe dissolution into the Zn–6Al–3Mg alloy melt, EDS composition analyses were carried out for the sample hot-dipped for 2 s. A representative result is presented in Fig. 5. The BEI (Fig. 5(a)) shows the interface between the IF steel sheet and the Zn alloy coating in the sample hot-dipped at 460°C for 2 s. Composition profiles across the interface are shown in Figs. 5(b) and 5(c). The location of the composition profile is indicated by a line in Fig. 5(a). The liquid Zn alloy was solidified into several  $\alpha$ -Al dendritic phases surrounded

by a fine eutectic microstructure (Fig. 5(a)). The observed solidified microstructure corresponds well to the prediction based on the calculated liquidus projection (as shown in Fig. 1). It is noteworthy that an Fe element with a relatively high content, above 3 at%, was detected inside the solidified Zn alloy melt close to the steel sheet (Fig. 5(c)). The concentration of Fe gradually decreases to approximately 2 at%, moving away from the steel sheet, indicating Fe dissolution into the Zn alloy melt even after 2 s of dipping. Note that Fe content in the used Zn alloy bath after all hot-dipping experiments was measured less than 0.1 at%.

### 3.2. Formation of Fe–Al Intermetallic Phases

Figure 6 displays BEIs showing the interfacial microstructure of IF steel sheets hot-dipped in the Zn–6Al–3Mg alloy melt at different temperatures for 2, 600, and 3600 s. Representative EDS element maps (corresponding to the BEI of the sample hot-dipped at 460°C for 600 s, as shown in Fig. 6(e)) are presented in Fig. 7. Microstructural characterizations revealed Fe–Al intermetallic phases at the interface between the Zn alloy melt and the steel sheet during the hot-dipping (as indicated by Figs. 6(e) and 7). The formation and growth of the Fe–Al intermetallic phases varied depending on the dipping temperature (Fig. 6). Fe–Al intermetallic phases were hardly observed in the sample hot-dipped at 400°C for 2 s in SEM resolution level (Fig. 6(g)), which corresponds well to the observed microstructures of Zn–Al–Mg alloy coatings on commercial hot-dip galvanized steels [14]. However, an Fe–Al intermetallic phase layer consisting of several grains elongated along the normal direction (ND) to the surface was observed in the sample hot-dipped for 600 s (Fig. 6(h)). The thickness of the Fe–Al intermetallic phase layer increased after hot-dipping for 3600 s (Fig. 6(i)). In the sample hot-dipped at 460°C for 2 s (Fig. 6(d)), Fe–Al intermetallic phases were also hardly observed. However, coarse Fe–Al intermetallic phases were locally formed on the thin layer after 600 s (Fig. 6(e)). The intermetallic phase grows toward both domains of the liquid Zn alloy and solid Fe, but it appears to

preferentially grow along the grain boundaries of the  $\alpha$ -Fe solid phase. The growth occurs more significantly after long-term dipping, resulting in the formation of numerous coarse particles of Fe–Al intermetallic phases surrounded by the liquid Zn alloy (solidified eutectic microstructure) in the sample hot-dipped for 3600 s (Fig. 6(f)). Such interfacial reaction, including the growth of the Fe–Al intermetallic phase, occurs earlier at 500°C [Figs. 6(b) and 6(c)]. Growth toward solid Fe appears to be more pronounced at higher temperatures. These observations agree with the significant thickness loss of the steel sheet hot-dipped at 500°C (Fig. 4).

Figure 8 presents high-magnification BEIs and corresponding EDS element maps for the thin Fe–Al intermetallic phase layer on the samples hot-dipped in the Zn–6Al–3Mg alloy melt for 2 s at 400 and 460°C. This high-magnification view (Fig. 8(a)) clearly shows a thin layer with dark contrast (as indicated by an arrowhead in Fig. 8(a)) on the IF steel sheet hot-dipped at 460°C. The observed thin layer is rich in Al (Fig. 8(b)), indicating a thin Fe–Al intermetallic phase layer with a thickness below 0.5  $\mu\text{m}$ . Overall, these results indicate that a thin Fe–Al intermetallic phase layer is initially formed at an early stage of dipping at 460°C, followed by a significant growth of the intermetallic phase after long-term dipping (as shown in Figs. 6(e) and 6(f)). Such Fe–Al intermetallic phases were not recognized in the sample hot-dipped at 400°C for 2 s (Figs. 8(d)–8(f)). Note that the Fe–Al intermetallic phase layer (with a thickness below 0.5  $\mu\text{m}$ ) was observed on the steel sheet hot-dipped for 60 s, indicating the growth of the intermetallic phase layer during dipping at the lowest temperature tested (i.e., 400°C) (as shown in Figs. 6(h) and 6(i)).

### 3.3. Phase Identification

Figure 9 presents the XRD profiles of the samples hot-dipped at different temperatures for 3,600 s. Diffraction peaks derived from  $\alpha$ -Fe (bcc) and  $\eta$ -Zn (hcp) phases were detected in all samples, which can be attributed to the steel sheet and the solidified Zn alloy melt in the coating, respectively. Diffraction



peaks attributed to the  $\eta$ -Fe<sub>2</sub>Al<sub>5</sub> phase [22] were observed in the XRD profiles obtained in the samples hot-dipped at 500 and 460°C (Figs. 9(a) and 9(b)). Higher peak intensities for the  $\eta$ -Fe<sub>2</sub>Al<sub>5</sub> phase were found in the samples hot-dipped at 500°C (Fig. 9(a)). These results demonstrate a coarsened Fe–Al intermetallic phase in the Zn alloy coating, corresponding to the  $\eta$ -Fe<sub>2</sub>Al<sub>5</sub> phase [Figs. 6(c) and 6(f)]. Note that diffraction peaks derived from Zn<sub>2</sub>Mg phase [19] rather than Zn<sub>11</sub>Mg<sub>2</sub> [18] phase were detected in the studied samples (Figs. 9(a) and 9(b)), suggesting the fine solidification microstructure consisting of  $\eta$ -Zn (hcp),  $\alpha$ -Al (fcc) and Zn<sub>2</sub>Mg phases in the Zn–6Al–3Mg alloy coating. The result corresponds well to previous studies [14].

Figure 10 shows representative results from the EBSD analyses carried out for the locally coarsened Fe–Al intermetallic phase on the IF steel hot-dipped at 460°C for 600 s (Fig. 10(a)). The analyzed EBSD patterns (Figs. 10(b)–10(g)) indicate the formation of a locally coarsened  $\eta$ -Fe<sub>2</sub>Al<sub>5</sub> phase in the sample. The confidence index (CI) value [23], which is used to evaluate the accuracy of indexing EBSD patterns, is 0.24, indicating the high reliability of the present analyzed results. It was also found that the  $\eta$  phase grows toward both domains of the liquid Zn alloy and solid  $\alpha$ -Fe. In order to determine the orientation of the  $\eta$  phase growth toward the solid Fe domain, EBSD scanning analyses were carried out. The result is presented in Fig. 11. The orientations of the  $\eta$  and  $\alpha$ -Fe phases were analyzed in the observed sample (Figs. 11(c) and 11(d)), and no clear EBSD pattern was obtained from the Al (fcc), Zn (hcp), and Zn<sub>2</sub>Mg phases in the fine solidification microstructure of the Zn alloy melt (Fig. 11(b)). The orientation color map for the  $\eta$  phase (Fig. 11(c)) indicates elongated grains to the ND in a particular direction close to the [001] plane orientation along the ND, suggesting a preferential growth of the  $\eta$  phase toward the solid Fe domain. In the  $\eta$  phase close to the liquid Zn alloy domain, relatively equiaxed grains were observed. In the  $\alpha$ -Fe phase adjacent to the  $\eta$  phase, significant orientation changes were localized around the interface between the  $\alpha$ -Fe and the  $\eta$  phases [Fig. 11(d)], indicating local straining in the  $\alpha$ -Fe phase close to the growing  $\eta$  phase. These

crystallographic features have also been observed in the  $\eta$  phase growing at the interface between solid Fe and liquid Al [24, 25]. Note that the same EBSD analysis for the sample hot-dipped at 460°C for 3600 s (Fig. 6(f)) revealed numerous  $\eta$  phase coarsened particles formed in the Zn alloy melt after long-term dipping.

In order to characterize the thin Fe–Al intermetallic phase layer observed in the samples hot-dipped at 400°C (Figs. 6(h) and 6(i)), EBSD analyses were carried out; the results are shown in Fig. 12. Clear EBSD patterns (Figs. 12(b) and 12(e)) were obtained from different locations within the thin Fe–Al intermetallic phase layer (as indicated by positions A and B in Fig. 12(a)). The EBSD patterns (Figs. 12(b)–12(g)) suggest that the observed thin layer consists of a  $\theta$ -Fe<sub>4</sub>Al<sub>13</sub> phase [26], with CI values above 0.14, indicating high reliability for the present phase identification. Note that these patterns (Figs. 12(b) and 12(e)) indicate different orientations, suggesting that the observed thin  $\theta$  phase layer consists of multiple grains.

## 4. Discussion

### 4.1 Formation of intermetallic phases in Zn–6Al–3Mg alloy melt

In the present study, we investigated Fe–Al intermetallic phases formed on IF steel hot-dipped in a Zn–6Al–3Mg alloy melt at various temperatures for different durations, revealing a pronounced growth of the  $\eta$ -Fe<sub>2</sub>Al<sub>5</sub> phase toward both directions of solid Fe and liquid Zn sides, at a dipping temperature above 460°C (Figs. 6 and 10). The observed morphology of the  $\eta$  phase agrees well with previous results for steel sheets hot-dipped in various Zn–Al–Mg alloy melts [8, 12]. In the samples hot-dipped at the lowest temperature tested (i.e., 400°C), a thin  $\theta$ -Fe<sub>3</sub>Al<sub>14</sub> phase layer was observed (Fig. 12), which suggests that a  $\theta$  phase is initially formed at the interface between the solid Fe and liquid Zn alloys. The locally coarsened  $\eta$  phase on the thin Fe–Al intermetallic phase layer (Figs. 7 and 10) evidences an initial  $\theta$  phase layer formation, followed by a pronounced growth of the  $\eta$  phase during the hot-dipping process. It is noteworthy that numerous

coarsened  $\eta$  phases (Figs. 6 and 9) were observed in the Zn alloy coating on the IF steel sheet with a substantially reduced thickness (Fig. 3). This clearly indicates an enhanced interfacial reaction corresponding to the formation of the  $\eta$  phase and the dissolution of Fe into the Zn alloy melt. The interfacial reaction and its related formation of  $\eta$  phase will be discussed utilizing the thermodynamic assessment of a Zn–Mg–Al–Fe quaternary system as follows.

Thermodynamic equilibrium calculations of the Zn–Mg–Al–Fe quaternary system were performed using the CALPHAD approach [27] based on previously reported thermodynamic databases [17, 28, 29]. The calculated result is presented in Fig. 13(a). In the calculated section of the Zn–Mg–Al–Fe quaternary phase diagram (Fig. 13(a)), the vertical and horizontal axes indicate the temperature and Fe content (at%), respectively. The origin on the horizontal axis corresponds to the alloy composition of Zn–12.8Al–7.1Mg (at%) (Zn–6Al–3Mg (wt.%)) in this figure. The thermodynamic assessment presents the appearance of the  $\theta$ -Fe<sub>4</sub>Al<sub>13</sub> phase in equilibrium with the liquid phase by increasing the Fe content in the studied Zn–6Al–3Mg alloy at elevated temperatures, ranging from 400 to 500°C. The assessment indicates the initial formation of a  $\theta$ -Fe<sub>4</sub>Al<sub>13</sub> phase enhanced by Fe dissolution in the Zn–6Al–3Mg alloy melt, in agreement with the present observations (Figs. 8 and 12). It is noteworthy that the two-phase region of  $\theta$  and liquid phases changes into the three-phase region of  $\theta$ , liquid and  $\eta$ -Fe<sub>2</sub>Al<sub>5</sub> phases by increasing the Fe content (Fig. 13(a)). Above 5 at% Fe content, a two-phase region of  $\eta$  phase and liquid phase appears at dipping temperatures, suggesting that the initially formed  $\theta$  phase could indeed transform to an  $\eta$  phase by increasing the Fe content in the Zn–6Al–3Mg alloy melt, in agreement with the current observation of locally coarsened  $\eta$  phase during the dipping process (Figs. 6 and 7). These reasonably good agreements with the experimental results could provide a conclusion that the  $\eta$  phase is likely formed via the transformation of the  $\theta$  to the  $\eta$  phase, which then substantially grows in the Zn–6Al–3Mg alloy melt after the long-term dipping.

Based on these findings, a possible mechanism for the interfacial reaction

between the liquid Zn–6Al–3Mg alloy and solid  $\alpha$ -Fe phase and its related formation sequence of Fe–Al intermetallic phases is discussed below. Schematics showing the formation process of Fe–Al intermetallic phases at the interface during dipping are illustrated in Figs. 13(b)–13(e). It is reasonable to consider the Fe dissolution into the liquid Zn alloy as a starting point for the reaction (as indicated in Fig. 5), because of the much higher diffusion rate in the liquid than in the solid (Fig. 13(b)). The Fe dissolution could provide Fe supersaturation in the Zn alloy melt close to the steel sheet, resulting in  $\theta$ -Fe<sub>4</sub>Al<sub>13</sub> phase nucleation. The  $\theta$  phase forms a continuous layer on the solid  $\alpha$ -Fe phase (Fig. 13(c)). The continuous  $\theta$  phase layer may play a role as a diffusion-controlling factor, resulting in the continuous growth of the  $\theta$  phase layer during dipping at the lowest temperature tested herein (i.e., 400°C) (Fig. 12). At higher temperatures, the initially formed  $\theta$  phase could be followed by the local formation of an  $\eta$  phase through a solid–solid reaction between the  $\theta$  and  $\alpha$ -Fe (IF steel sheet) phases (Fig. 13(d)). This corresponds to a transition from a two-phase region of  $\theta$  and liquid phases to a three-phase region of  $\eta$ ,  $\theta$ , and liquid phases (Fig. 13(a)) by increasing the Fe content around the interface between the  $\theta$  and  $\alpha$ -Fe phases. The  $\eta$  phase grows toward both the liquid Zn alloy and the solid Fe domains after further dipping (Fig. 13(e)), resulting in the local growth of the  $\eta$  phase observed in the present study (Fig. 10). The possible  $\theta \rightarrow \eta$  transformation might accompany a volume contraction of approximately 8% under the assumption that the difference in the lattice parameters between the  $\theta$  and the  $\eta$  phase measured at room temperature [22, 26] is the same as at the dipping temperatures. The local straining caused by the  $\theta \rightarrow \eta$  transformation could lead to cracking inside the initially formed  $\theta$  phase layer, which enhances the Fe dissolution into the Zn alloy melt through the solid–liquid interface (solid  $\alpha$ -Fe in contact with the liquid Zn alloy). The enhanced Fe dissolution could provide the driving force for the growth of the  $\eta$  phase in the liquid Zn alloy, resulting in the formation of the observed coarse particles of the  $\eta$  phase in the Zn alloy melt after long-term dipping (Figs. 6(c) and 6(f)). Note that the transition from a two-phase region of  $\theta$  and liquid

phases to a three-phase region of  $\eta$ ,  $\theta$ , and liquid phases is located around 3.5 at% Fe content at a temperature range of 400–500°C in the calculated Zn–Mg–Al–Fe quaternary phase diagram (Fig. 13(a)). The calculation predicts that the formation sequence of Fe–Al intermetallic phases is independent of the dipping temperature. It can, therefore, be considered that the local growth of the  $\eta$  phase would occur at the lowest temperature of 400°C after further long-term dipping.

The proposed interfacial process mentioned above requires the understanding of the Fe dissolution process in the Zn alloy melt. It is generally understood the solubility of Fe in liquid Zn alloys provides the driving force for Fe dissolution. The present thermodynamic assessment in the Zn–Mg–Al–Fe quaternary system predicts a limited Fe solubility below 0.02 at% in the liquid phase with a composition of Zn–6Al–3Mg (wt.%). However, a much higher Fe content in the Zn alloy melt was experimentally measured in the sample hot-dipped for 2 s (Fig. 5), suggesting higher solubility limits of Fe at dipping temperatures ranging from 400°C to 500°C. In order to reveal the detailed mechanism of the interfacial reaction process, further research is needed to better understand the phase equilibria among the  $\theta$  and liquid phases and the associated solubility limits of Fe in the liquid phase in the Zn–Mg–Al–Fe quaternary system.

#### **4.2 Effect of alloy elements on the formation of intermetallic phases**

Based on the above-mentioned mechanism, the effect of alloy elements (Al and Mg) in the Zn alloy melt on the formation of Fe–Al intermetallic phases will be discussed utilizing the calculated phase diagram of a Zn–Mg–Al–Fe quaternary system below. Figure 14 presents various calculated sections of the Zn–Mg–Al–Fe quaternary phase diagram. In these figures, the origins on the horizontal axis correspond to the Zn alloy compositions of Zn–0.2Al–3Mg, Zn–1Al–3Mg and Zn–2Al–3Mg (wt.%). The calculated Zn–0.2Al–3Mg–Fe section (Fig. 14(a)) indicates the  $\eta$ -Fe<sub>2</sub>Al<sub>5</sub> phase in equilibrium with the liquid phase by increasing the Fe content at dipping temperatures ranging from 400°C to 500°C, indicating the initially formed  $\eta$  phase rather than  $\theta$  phase in a Zn–0.2Al–3Mg (wt.%) alloy melt.

The assessment corresponds well to the previous results on the hot-dip Zn–0.2Al alloy coated steels [30, 31]. The calculated Zn–1Al–3Mg–Fe and Zn–2Al–3Mg–Fe sections (Figs. 14(b) and 14(c)) represent a larger two-phase region of  $\theta$  and liquid phases in the higher Al content alloy melt, which is indicative of  $\theta$  phase stabilized by Al element in the Zn–Al–Mg alloy melt. These assessments imply the formation sequence of Fe–Al intermetallic phases would change depending on Al content in the Zn–Al–Mg alloy bath used for hot-dip galvanizing process.

Figure 15 shows a calculated section of 1 wt.% Fe at 460°C in the Zn–Mg–Al–Fe quaternary phase diagram. The labeled phases could correspond to the initially formed phases on the steel sheets hot-dipped in the Zn–Mg–Al alloy melts. The calculated section indicates a slight effect of Mg content on the formation of initial phases in the dipping at 460°C, although  $Zn_2Mg$  phase would appear in higher Mg content. Xie et al. demonstrated that Mg content in the Zn–Al–Mg alloy melt inhibited the formation of the Fe–Al intermetallic phase layer on the steels [12]. It was also found that Mg element segregated at the grain boundaries of the Fe–Al intermetallic phase layer [12]. These results suggest that segregated Mg element would contribute to the sluggish growth kinetics of the  $\eta$  phase in the Zn–Al–Mg alloy melt. It can be therefore considered that Mg content would have a slight effect on the formation sequence of Fe–Al intermetallic phases in the hot-dip Zn–Al–Mg alloy galvanizing process.

## 5. Summary

In this paper, we examined the formation of Fe–Al intermetallic phases on IF steel hot-dipped in a Zn–6Al–3Mg (wt.%) alloy melt (a commercial relevant coating alloy) at different temperatures (400–500°C) and dipping durations (2~3,600 s). The chemical composition analyses evidenced the dissolution of Fe into the Zn alloy melt even after 2 s of dipping. Microstructural characterization revealed that a continuous  $\theta$ - $Fe_4Al_{13}$  phase layer was initially formed, followed by the local growth of an  $\eta$ - $Fe_2Al_5$  phase toward both solid  $\alpha$ -Fe and liquid Zn alloy sides during the hot-dipping process. Further growth of the  $\eta$  phase accompanied

the dissolution of Fe into the Zn alloy melt, resulting in a significant thickness loss in the IF steel sheets during the hot-dipping process. These experimental results are in good agreement with the scenario of a phase transition from a two-phase region of  $\theta$  and liquid phases to a three-phase region of  $\eta$ ,  $\theta$ , and liquid phases by increasing the Fe content in the Zn–6Al–3Mg alloy, predicted by the calculated Zn–Al–Mg–Fe quaternary phase diagram.

## ACKNOWLEDGMENTS

The authors are grateful for the technical support given by Dr. S. Koga and Mr. K. Ishii (Nisshin Steel Co., Ltd.) with the sample preparation, and by Mr. K. Hashimoto (Materials Design Technology Co., Ltd.) with the thermodynamic assessments. The support of Hitachi Metals-Materials Science Foundation was gratefully acknowledged.

## REFERENCES

- [1] A. R. Marder, The metallurgy of zinc-coated steel, *Prog. Mater. Sci.* 45 (2000), 191–271.
- [2] D. Mizuno, Automotive Corrosion and Accelerated Corrosion Tests for Zinc Coated Steels, *ISIJ Int.* 58 (2018) 1562–1568.
- [3] T. Tsujimura, A. Komatsu, A. Andoh, Influence of Mg content in Coating Layer and Coating Structure on Corrosion Resistance of Hot-Dip Zn-Al-Mg Alloy Coated Steel Sheet, in: *Proceedings of International Conference on Zinc and Zinc Alloy Coated Steel (GALVATEC01)*, Brussels, Belgium, June 26–28, 2001, pp. 145–152.
- [4] S. Schuerz, M. Fleischanderl, G.H. Luckeneder, K. Preis, T. Haunschmied, G. Mori, A.C. Kneissl, Corrosion Behaviour of Zn–Al–Mg Coated Steel Sheet in Sodium Chloride-Containing Environment, *Corros. Sci.* 51 (2009) 2355–2363.
- [5] M. S. Azevedo, C. Allély, K. Ogle, P. Volovitch, Corrosion Mechanisms of Zn(Mg,Al) Coated Steel: 2. The Effect of Mg and Al Alloying on the Formation and Properties of Corrosion Products in Different Electrolytes, *Corros. Sci.* 90 (2015) 482–490.

- [6] T. Morooka, Application of the Hot-dip Zn–Al–Mg alloy Platin to the Steel Structure, in: Proceedings of 11<sup>th</sup> International Conference on Zinc and Zinc Alloy Coated Steel Sheet (GALVATECH2017), Nov. 12–16, Tokyo, Japan, 2017, pp. 338–343.
- [7] R.W. Richards, R.D. Jones, P.D. Clements, H. Clarke, Metallurgy of continuous hot dip aluminizing, *Inter. Mater. Rev.* 39 (1994) 191–212.
- [8] K. Honda, K. Ushioda, W. Yamada, Influence of Si Addition to the Coating Bath on the Growth of the Al–Fe Alloy Layer in Hot-dip Zn–Al–Mg Alloy-coated Steel Sheets, *ISIJ Int.* 51 (2011) 1895–1902.
- [9] Y. Chen, Y. Liu, H. Tu, C. Wu, X. Su, J. Wang, Effect of Ti on the Growth of the Fe–Al Layer in a Hot Dipped Zn–6Al–3Mg Coating, *Surf. Coat. Technol.* 275 (2015) 90–97.
- [10] K. Li, Y. Liu, H. Tu, X. Su, J. Wang, Effect of Si on the Growth of Fe–Al Intermetallic Layer in Zn–11%Al–3%Mg Coating, *Surf. Coat. Technol.* 306 (2016) 390–396.
- [11] J.-K. Chang, C.-S. Lin, Microstructural Evolution of 11Al–3Mg–Zn Ternary Alloy-Coated Steels During Austenitization Heat Treatment, *Metall. Mater. Trans. A* 48 (2017) 3734–3744.
- [12] Y. Xie, A. Du, X. Zhao, R. Ma, Y. Fa, X. Cao, Effect of Mg on Fe–Al Interface Structure of Hot–Dip Galvanized Zn–Al–Mg Alloy Coatings, *Surf. Coat. Technol.* 337 (2018) 313–320.
- [13] T. Tsukahara, N. Takata, S. Kobayashi, M. Takeyama, Mechanical Properties of Fe<sub>2</sub>Al<sub>5</sub> and FeAl<sub>3</sub> Intermetallic Phases at Ambient Temperature, *Tetsu-to-Hagané* 102 (2016) 89–95.
- [14] Y.B. Park, I.G. Kim, S.G. Kim, W.T. Kim, T.C. Kim, M.S. Oh, J.S. Kim, Orientation Dependence of Cracking in Hot-Dip Zn–Al–Mg Alloy Coatings on a Sheet Steel, *Metall. Mater. Trans. A* 48 (2017) 1013–1020.
- [15] A. Nishimoto, J. Inagaki, K. Nakaoka, Influence of Alloying Elements in Hot Dip Galvanized High Tensile Strength Sheet Steels on the Adhesion and Iron-zinc Alloying Rate, *Tetsu-to-Hagané*, 68 (1982), 1404–1410.
- [16] L. Chen, R. Fourmentin, J. R. McDermid, Morphology and Kinetics of Interfacial Layer Formation during Continuous Hot-Dip Galvanizing and Galvannealing, *Metall. Mater. Trans. A*, 39 (2008), 2128–2142.



- [17] P. Liang, T. Tarfa, J. A. Robinson, S. Wagner, P. Ochin, M. G. Harmelin, H. J. Seifert, H. L. Lukas, F. Aldinger, Experimental Investigation and Thermodynamic Calculation of the Al–Mg–Zn System, *Thermo. Acta* 314 (1998) 87–110.
- [18] S. Samson, Die Kristallstruktur von  $Mg_2Zn_{11}$ . Isomorphie zwischen  $Mg_2Zn_{11}$  und  $Mg_2Cu_6Al_5$  *Acta Chemica Scandinavica*, 3 (1949), 835-845.
- [19] L. Tarschisch, A. T. Titow, F. K. Garjanow, Röntgenpgraphische untersuchung der verbindung  $MgZn_2$ , *Physikalische Zeitschrift der Sowjetunion*, 5 (1934) 503–510.
- [20] N. Takata, M. Takeyama, Effect of Steel Microstructure on Solid Fe/Liquid Zn Interface Reaction in Hot-dipped Zn Galvanized Steels, *Tetsu-to-Hagané*, 100 (2014) 1172–1179.
- [21] N. Takata, K. Hayano, A. Suzuki, M. Kobashi, Enhanced Interfacial Reaction of Fe–Si Alloy Sheets Hot-Dipped in Zn Melt at 460°C, *ISIJ Int.* 58 (2018) 1608–1615.
- [22] U. Burkhardt, Y. Grin, M. Ellner, K. Peters, Structure Refinement of the Iron-Aluminium Phase with the Approximate Composition  $Fe_2Al_5$ , *Acta Cryst. B* 50 (1994) 313–316.
- [23] S. I. Wright, M. M. Nowell, S. P. Lindeman, P. P. Camus, M. D. Graef, M. A. Jackson, Introduction and Comparison of New EBSD Post-Processing Methodologies, *Ultramicroscopy* 159 (2015) 81–94.
- [24] N. Takata, M. Nishimoto, S. Kobayashi, M. Takeyama, Morphology and Formation of Fe–Al Intermetallic Layers on Iron Hot-Dipped in Al–Mg–Si Alloy Melt, *Intermetallics* 54 (2014) 136–142.
- [25] N. Takata, M. Nishimoto, S. Kobayashi, M. Takeyama, Crystallography of  $Fe_2Al_5$  Phase at the Interface between Solid Fe and Liquid Al, *Intermetallics* 67 (2015) 1–11.
- [26] P. J. Black, The Structure of  $FeAl_{3,1}$ , *Acta Cryst.* 8 (1955) 43–48.
- [27] Y. A. Chang, S. Chen, F. Zhang, X. Yan, F. Xie, R. Schmid-Fetzer, W. A. Oates, Phase Diagram Calculation: Past, Present and Future, *Prog. Mater. Sci.* 49 (2004) 313–345.
- [28] J. Nakano, D. V. Malakhov, G. R. Purdy, A crystallographically consistent optimization of the Zn–Fe system, *CALPHAD* 29 (2005) 276–288.
- [29] J. Nakano, D. V. Malakhov, S. Yamaguchi, G. R. Purdy, A full thermodynamic optimization of the Zn–Fe–Al system within the 420–500°C temperature range, *CALPHAD* 31 (2007) 125–140.

- [30] T. Kato, K. Nunome, K. Kaneko, S. Saka, Formation of the  $\zeta$  phase at an interface between an Fe substrate and a molten 0.2 mass% Al-Zn during galvannealing, *Acta Mater.* 48 (2000), 2257–2262.
- [31] N. Takata, K. Hayano, A. Suzuki, M. Kobashi, Formation of  $\text{Fe}_2\text{Al}_5$  Phase Layer on Fe–Si Alloy Sheets Hot-Dipped in Zn-0.2Al Alloy Melt, *Tetsu-to-Hagané* 105 (2019) in press.

## Caption List

**Figure 1** Composition of the studied Zn alloy melt plotted on the liquidus projection of a Zn–Al–Mg ternary phase diagram.

**Figure 2** Representative thermal profiles of the IF steel sheet during the hot-dip process. Dipping in the Zn alloy melt for 600 s at different temperatures: 400°C (solid black line), 460°C (gray line) and 500°C (dashed line).

**Figure 3** BEIs showing the cross section of the IF steel sheets hot-dipped in a Zn–6Al–3Mg (wt.%) alloy melt at (a–c) 500°C, (d–f) 460°C and (g–i) 400°C for (a, d, g) 2 s, (b, e, h) 600 s and (c, f, i) 3600 s.

**Figure 4** Change in the IF steel sheet ( $t_{Fe}$ ) thickness as a function of dipping time at 400°C (white circles), 460°C (gray circles) and 500°C (black circles).

**Figure 5** (a) BEIs showing the interfacial microstructure of IF steel sheets hot-dipped in a Zn–6Al–3Mg (wt.%) alloy melt at 460°C for 2 s and (b, c) the corresponding concentration line profiles across the interface between the steel sheet and solidified Zn alloy melt.

**Figure 6** BEIs showing the intermetallic phase on IF steel sheets hot-dipped in a Zn–6Al–3Mg (wt.%) alloy melt at (a–c) 500°C, (d–f) 460°C, and (g–i) 400°C for (a, d, g) 2 s, (b, e, h) 600 s, and (c, f, i) 3600 s.

**Figure 7** EDS element maps of the IF steel sheet hot-dipped in a Zn–6Al–3Mg (wt.%) alloy melt for 600 s at 460°C. These maps correspond to the BEI shown in Fig. 6(e).

**Figure 8** (a, d) High-magnification BEIs and (b, c, e, f) the corresponding element maps of Al and Fe for the IF steel sheets hot-dipped in a Zn–6Al–3Mg (wt.%) alloy melt for 2 s at (a–c) 460°C and (d–f) 400°C.

**Figure 9** XRD profiles of IF steel sheets hot-dipped for 3,600 s in a Zn–6Al–3Mg (wt.%) alloy melt at (a) 500°C, (b) 460°C and (c) 400°C.

**Figure 10** (a) BEIs showing the coarsened intermetallic phase on IF steel sheets hot-dipped in a Zn–6Al–3Mg (wt.%) alloy melt at 460°C for 600 s, (b, e) EBSD patterns obtained from the locations of A and B in (a), and (c, d, f, g) the analyzed EBSD patterns using

the crystal structure of the  $\eta$ -Fe<sub>2</sub>Al<sub>5</sub> phase (*oC24*) [22].

**Figure 11** (a) SEM image showing the Fe–Al intermetallic phase on IF steel sheets hot-dipped in a Zn–6Al–3Mg (wt.%) melt at 460°C for 600 s and (b) the corresponding phase map and (c, d) orientation color maps of the (c)  $\eta$ -Fe<sub>2</sub>Al<sub>5</sub> and (d)  $\alpha$ -Fe phases. The color represents the ND orientation according to the orientation color key in the attached unit triangles.

**Figure 12** (a) SEM image showing the intermetallic phase layer on IF steel sheets hot-dipped in a Zn–6Al–3Mg (wt.%) alloy melt at 400°C for 3,600 s, (b, e) EBSD patterns obtained from the locations of A and B in (a), and (c, d, f, g) the analyzed EBSD patterns using the crystal structure of the  $\theta$ -Fe<sub>4</sub>Al<sub>13</sub> phase (*mS102*) [26].

**Figure 13** (a) Calculated section of the Zn–Mg–Al–Fe quaternary phase diagram. In this section, the vertical and horizontal axes indicate the temperature and Fe content (at%), respectively. The origin on the horizontal axis corresponds to the studied alloy composition of Zn–12.8Al–7.1Mg (at%) (Zn–6Al–3Mg (wt.%)). (b–e) Schematics showing the interfacial reaction between the liquid Zn–6Al–3Mg (wt.%) and solid  $\alpha$ -Fe phases corresponding to the phase transition presented in (a).

**Figure 14** Calculated sections of the Zn–Mg–Al–Fe quaternary phase diagram. In this section, the vertical and horizontal axes indicate the temperature and Fe content (wt.%), respectively. The origin on the horizontal axis corresponds to the different compositions of (a) Zn–0.2Al–3Mg, (b) Zn –1Al–3Mg and (c) Zn–2Al–3Mg (wt.%).

**Figure 15** Calculated section of 1 wt.% Fe at 460°C in the Zn–Mg–Al–Fe quaternary phase diagram.

**Table 1** Chemical composition of the studied IF steel sheets (wt.%).

**Table 1** Chemical composition of the IF steel sheet studied (wt%).

C	Si	Mn	P	S	Al	Ti	Nb	Cr	Cu	Ni	Fe
0.003	0.006	0.150	0.015	0.009	0.039	0.058	0.000	0.030	0.020	0.010	Bal.

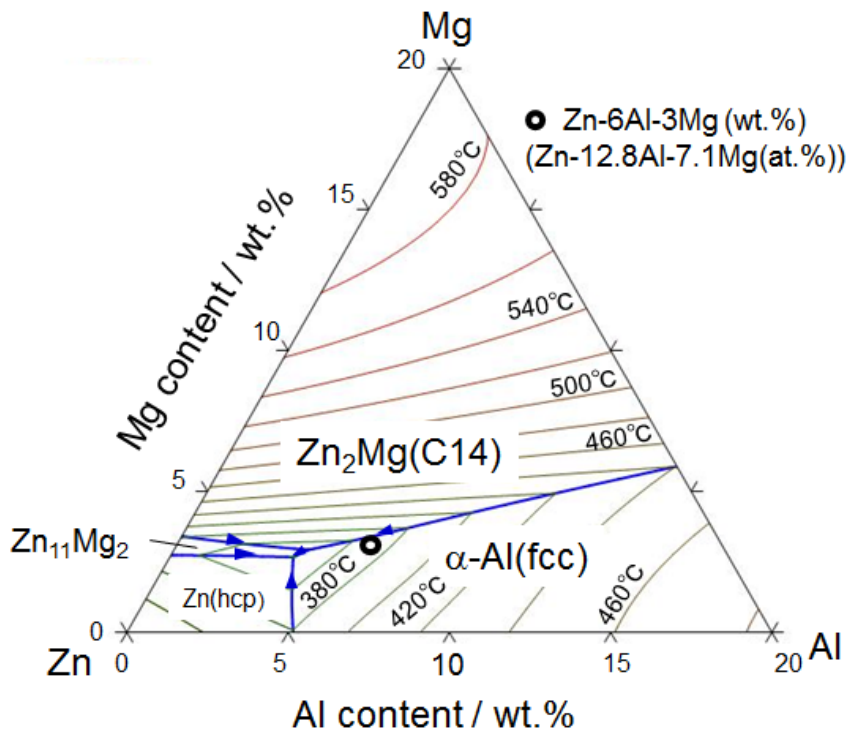


**Figure 1** Composition of the studied Zn alloy melt plotted on the liquidus projection of a Zn–Al–Mg ternary phase diagram.

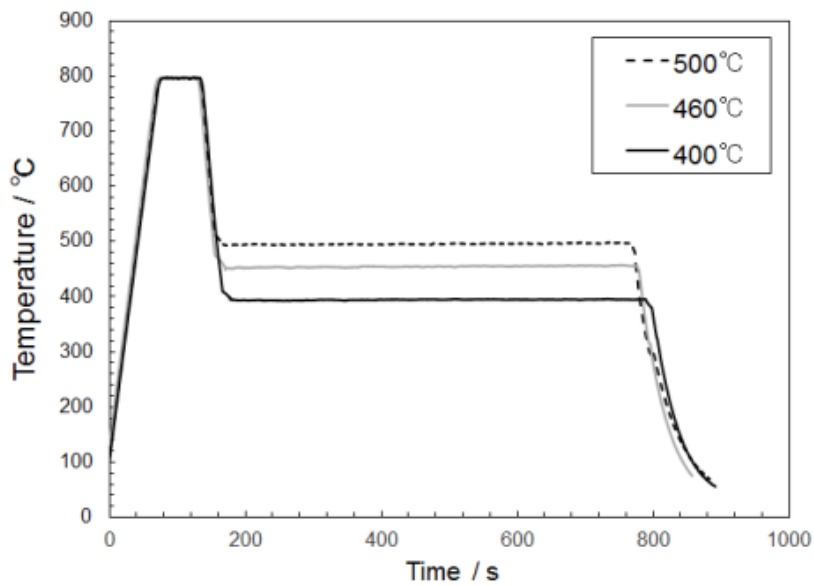


**Figure 2** Representative thermal profiles of the IF steel sheet during the hot-dip process. Dipping in the Zn alloy melt for 600s at different temperatures: 400 °C (solid black line), 460 °C (gray line), and 500 °C (dashed line).

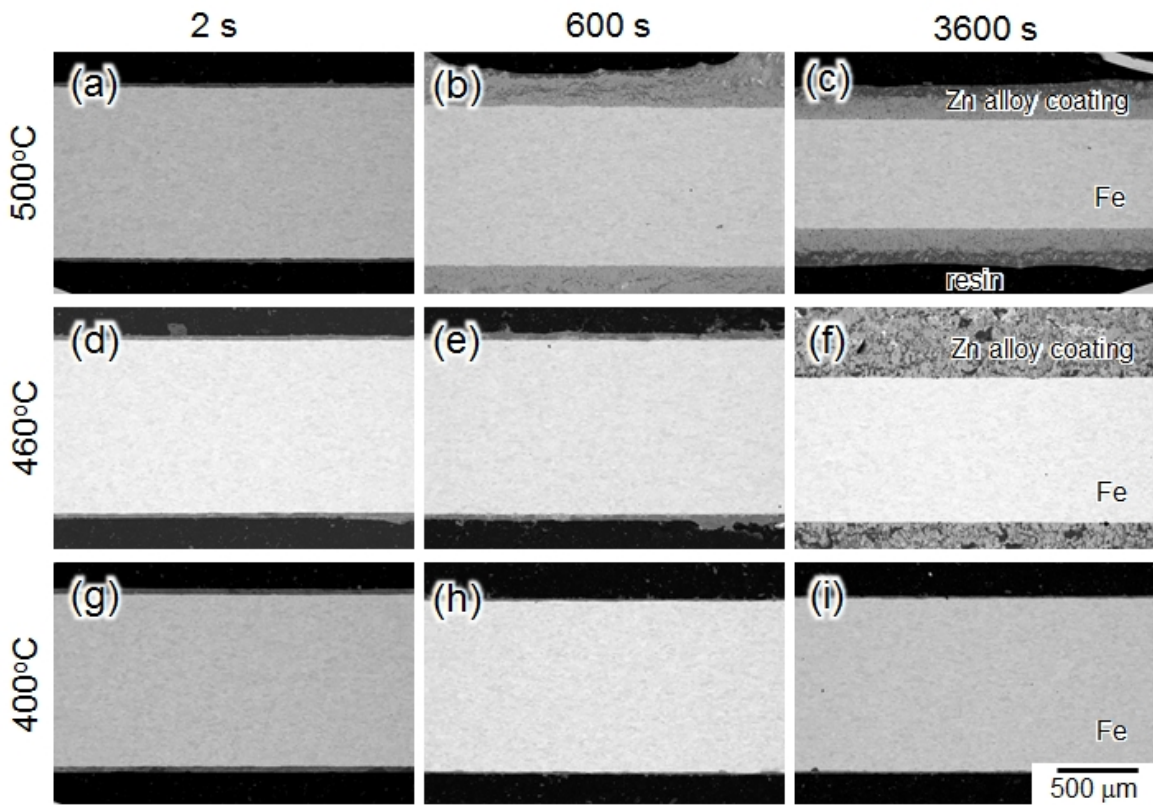


**Figure 3** BEIs showing the cross section of the IF steel sheets hot-dipped in a Zn–6Al–3Mg (wt.%) alloy melt at (a–c) 500 °C, (d–f) 460 °C, and (g–i) 400 °C for (a, d, g) 2s, (b, e, h) 600s, and (c, f, i) 3600s.



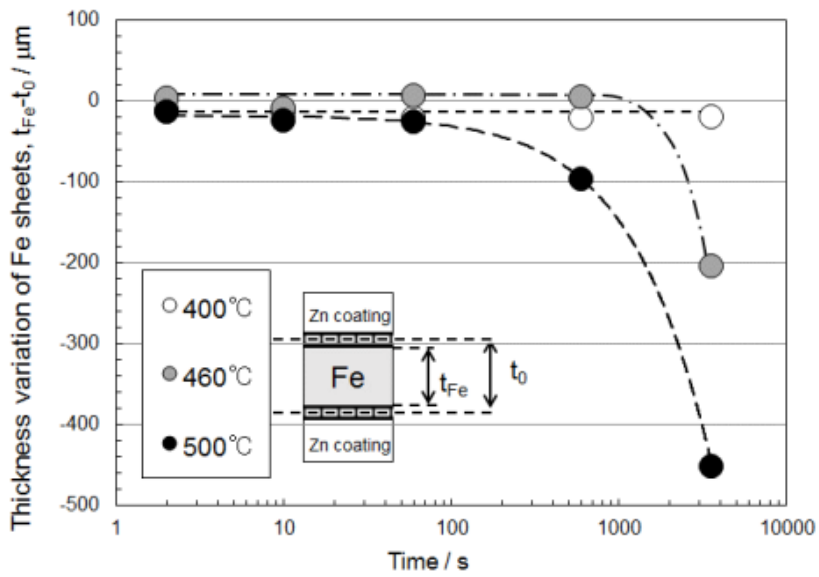


**Figure 4** Change in the IF steel sheet ( $t_{Fe}$ ) thickness as a function of dipping time at 400 °C(white circles), 460 °C (gray circles) and 500 °C(black circles).

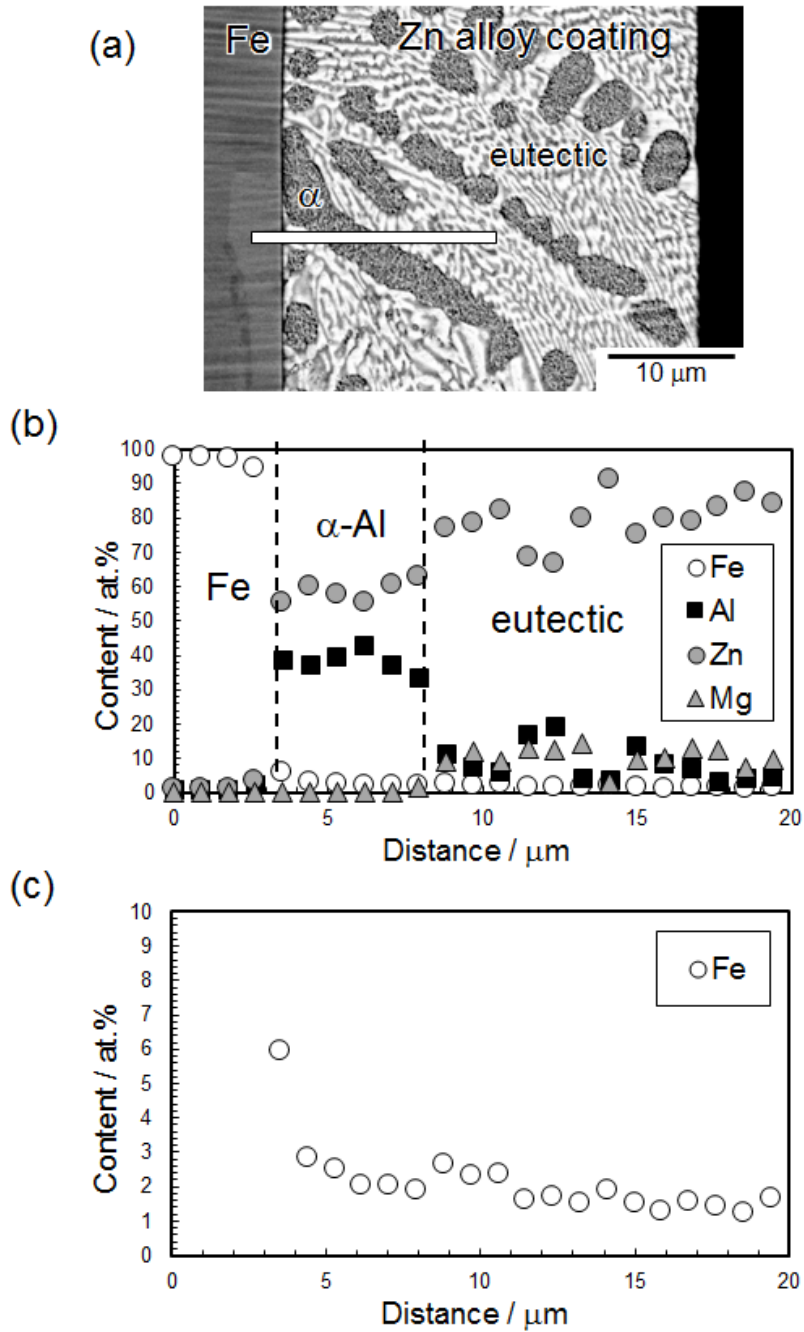


**Figure 5** (a) BEIs showing the interfacial microstructure of IF steel sheets hot-dipped in a Zn–6Al–3Mg (wt.%) alloy melt at 460°C for 2 s and (b, c) the corresponding concentration line profiles across the interface between the steel sheet and solidified Zn alloy melt.

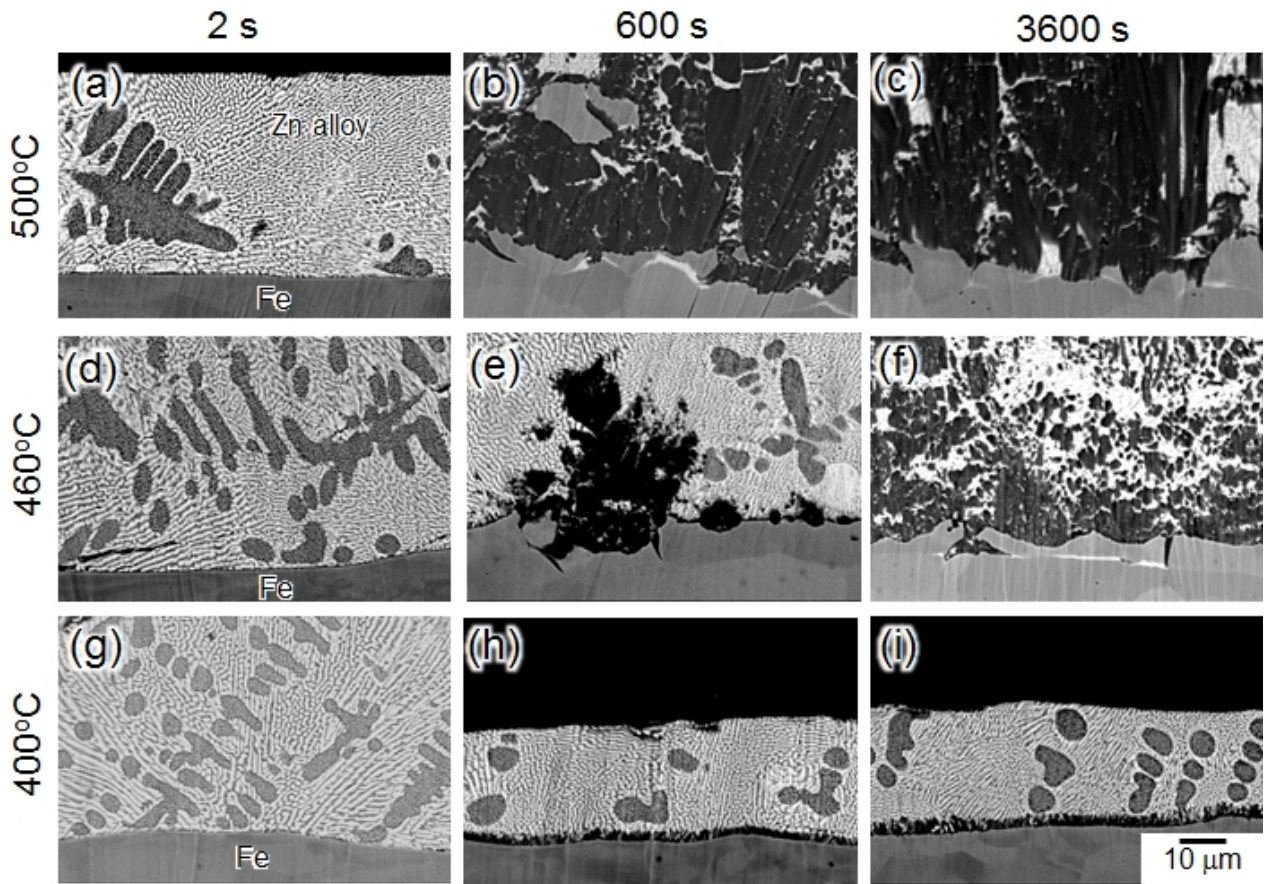


**Figure 6** BEIs showing the intermetallic phase on IF steel sheets hot-dipped in a Zn-6Al-3Mg (wt.%) alloy melt at (a–c) 500°C, (d–f) 460°C, and (g–i) 400°C for (a, d, g) 2s, (b, e, h) 600s, and (c, f, i) 3600s.

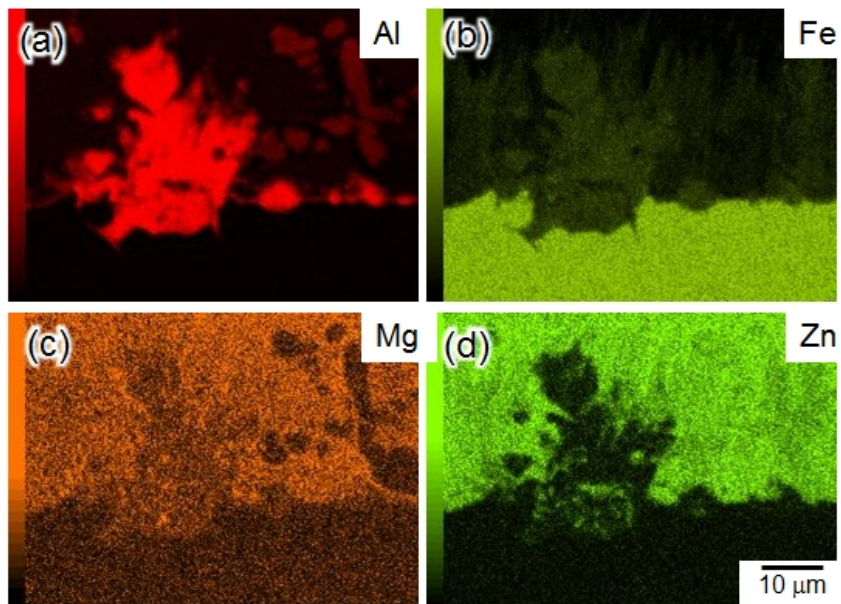


**Figure 7** EDS element maps of the IF steel sheet hot-dipped in a Zn–6Al–3Mg (wt.%) alloy melt for 600s at 460°C. These maps correspond to the BEI shown in Fig. 6(e).

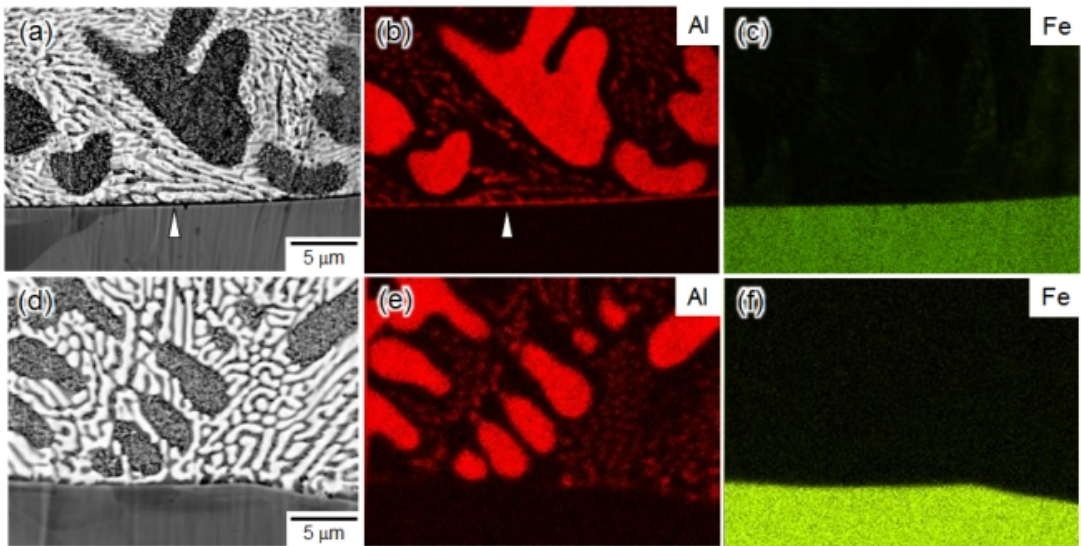


**Figure 8** (a, d) High-magnification BEIs and (b, c, e, f) the corresponding element maps of Al and Fe for the IF steel sheets hot-dipped in a Zn-6Al-3Mg (wt.%) alloy melt for 2s at (a-c) 460°C and (d-f) 400°C.

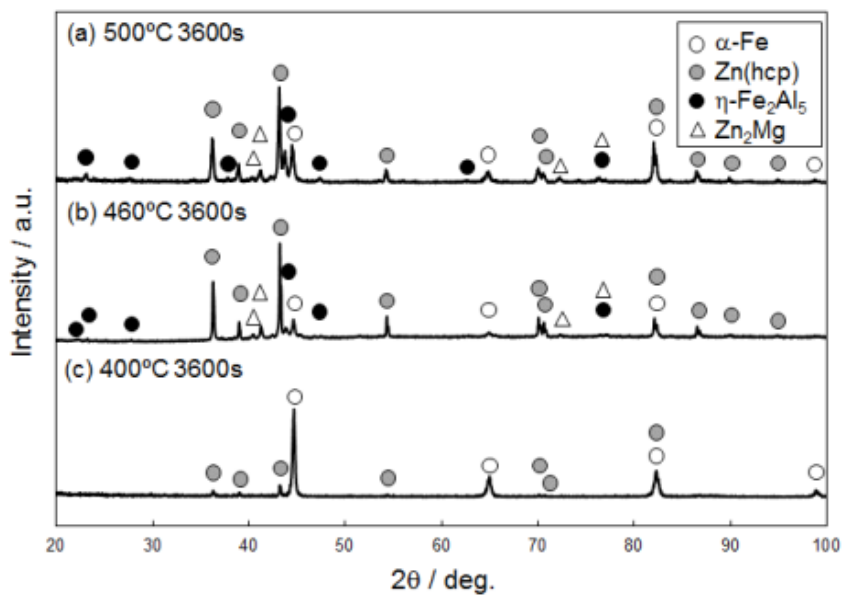


**Figure 9** XRD profiles of IF steel sheets hot-dipped for 3600s in a Zn–6Al–3Mg (wt.%) alloy melt at (a) 500°C, (b) 460°C and (c) 400°C.



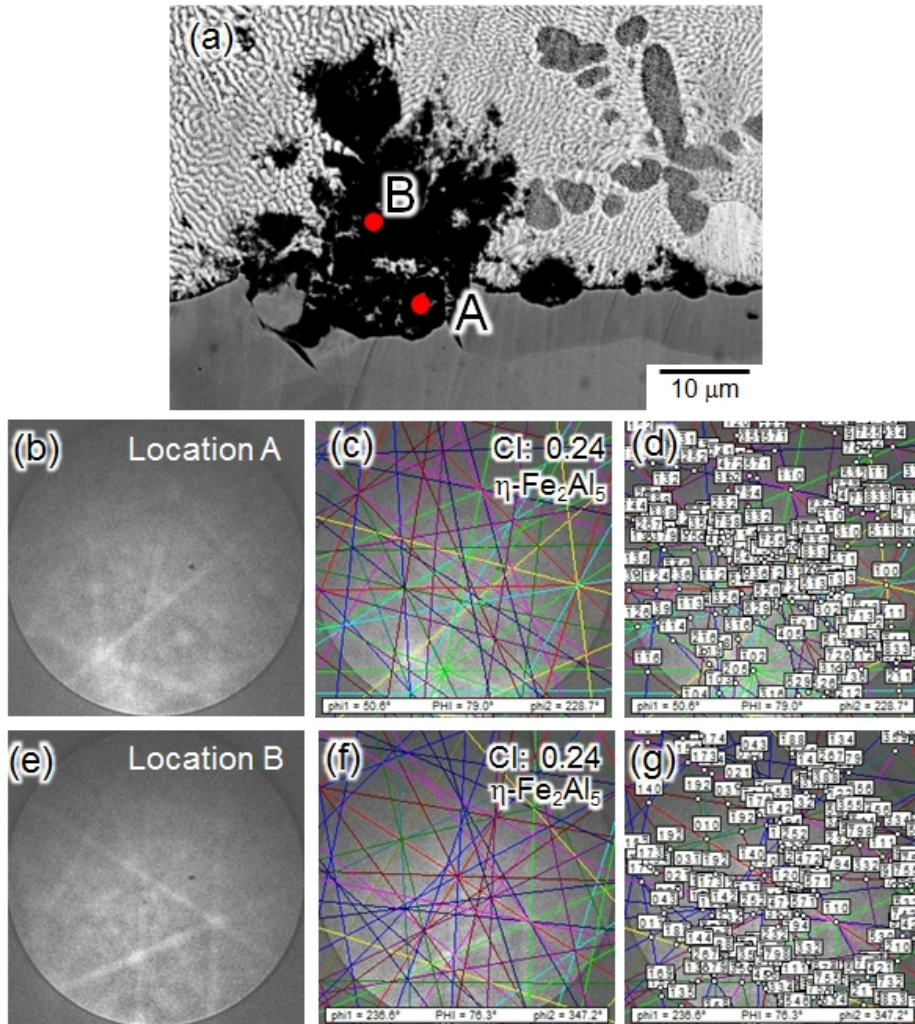


**Figure 10** (a) BEIs showing the coarsened intermetallic phase on IF steel sheets hot-dipped in a Zn–6Al–3Mg (wt.%) alloy melt at 460°C for 600s, (b, e) EBSD patterns obtained from the locations of A and B in (a), and (c, d, f, g) the analyzed EBSD patterns using the crystal structure of the  $\eta$ -Fe<sub>2</sub>Al<sub>5</sub> phase (*oC24*) [22].

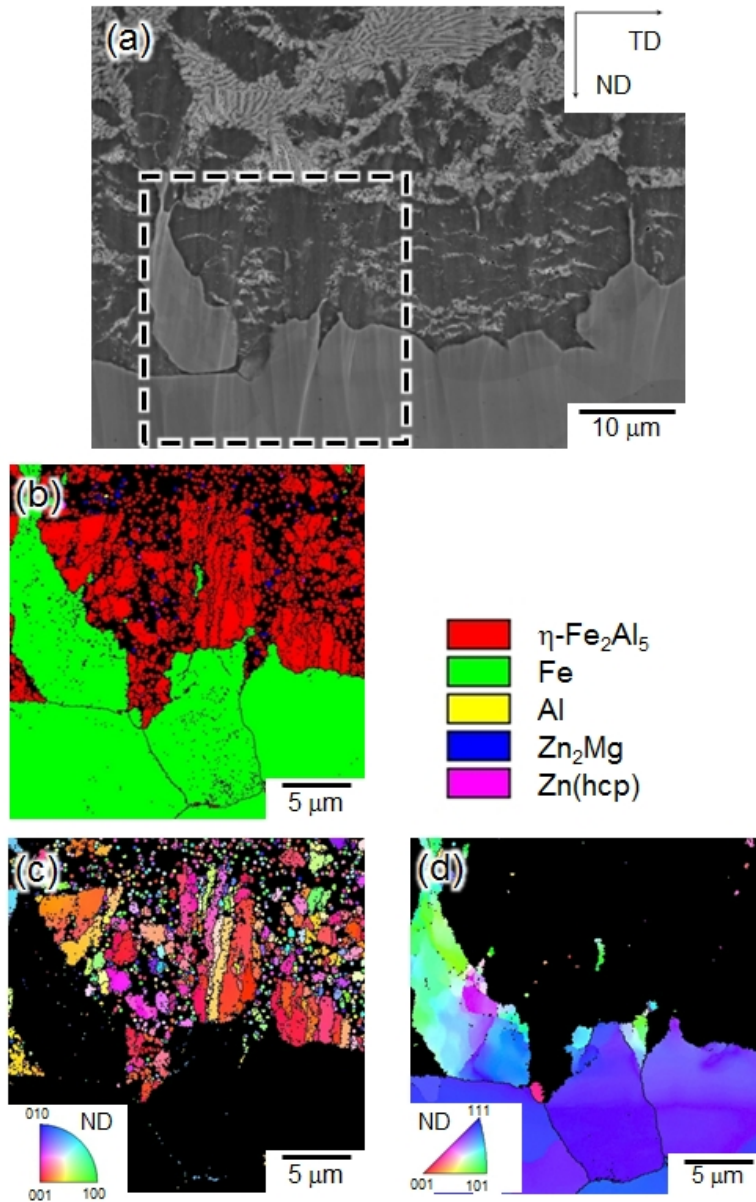


**Figure 11** (a) SEM image showing the Fe–Al intermetallic phase on IF steel sheets hot-dipped in a Zn–6Al–3Mg (wt.%) melt at 460°C for 600s and (b) the corresponding phase map and (c, d) orientation color maps of the (c)  $\eta$ -Fe<sub>2</sub>Al<sub>5</sub> and (d)  $\alpha$ -Fe phases. The color represents the ND orientation according to the orientation color key in the attached unit triangles.



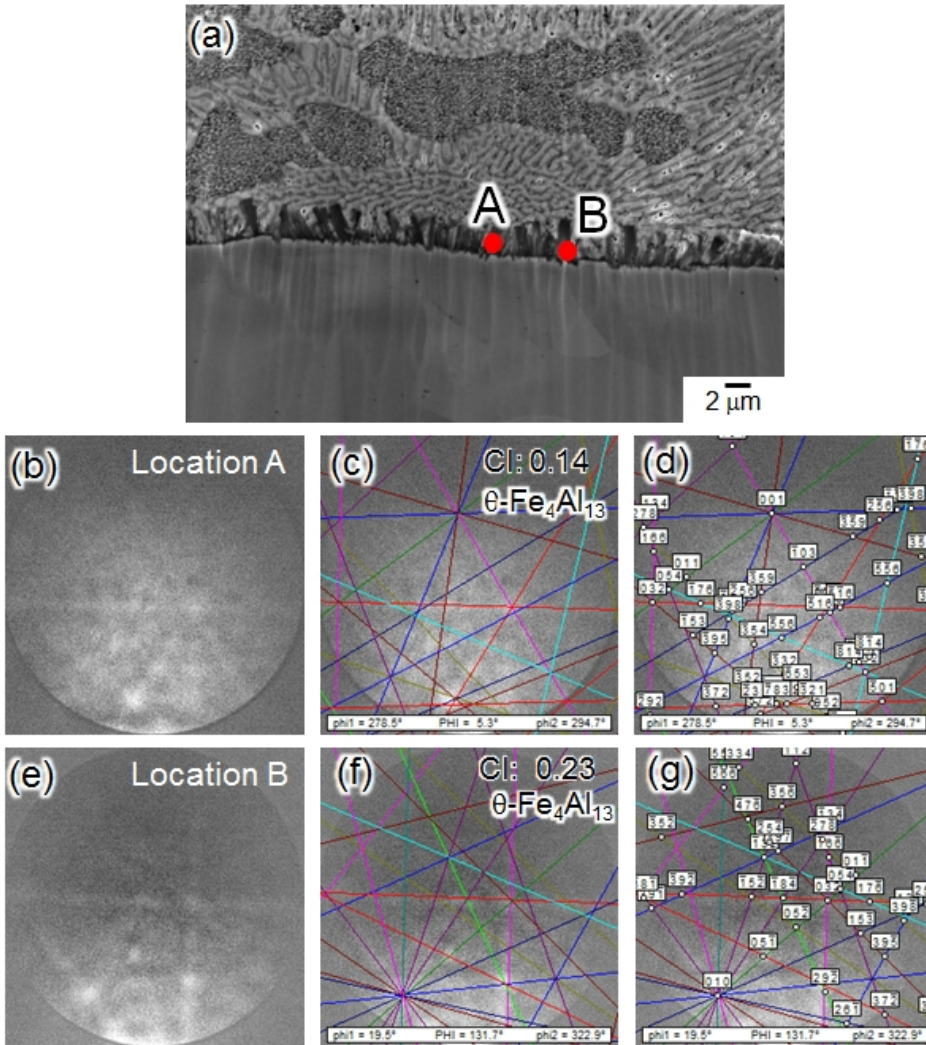


**Figure 12** (a) SEM image showing the intermetallic phase layer on IF steel sheets hot-dipped in a Zn–6Al–3Mg (wt.%) alloy melt at 400°C for 3600s, (b, e) EBSD patterns obtained from the locations of A and B in (a), and (c, d, f, g) the analyzed EBSD patterns using the crystal structure of the  $\theta$ -Fe<sub>4</sub>Al<sub>13</sub> phase (mS102) [26].

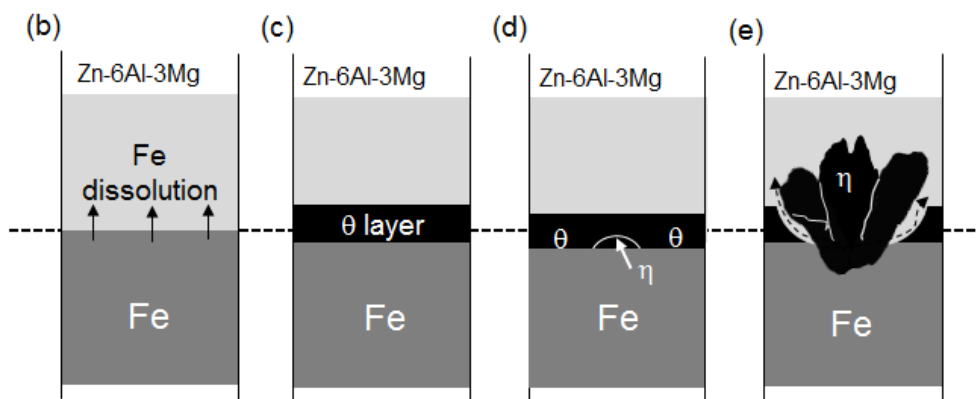
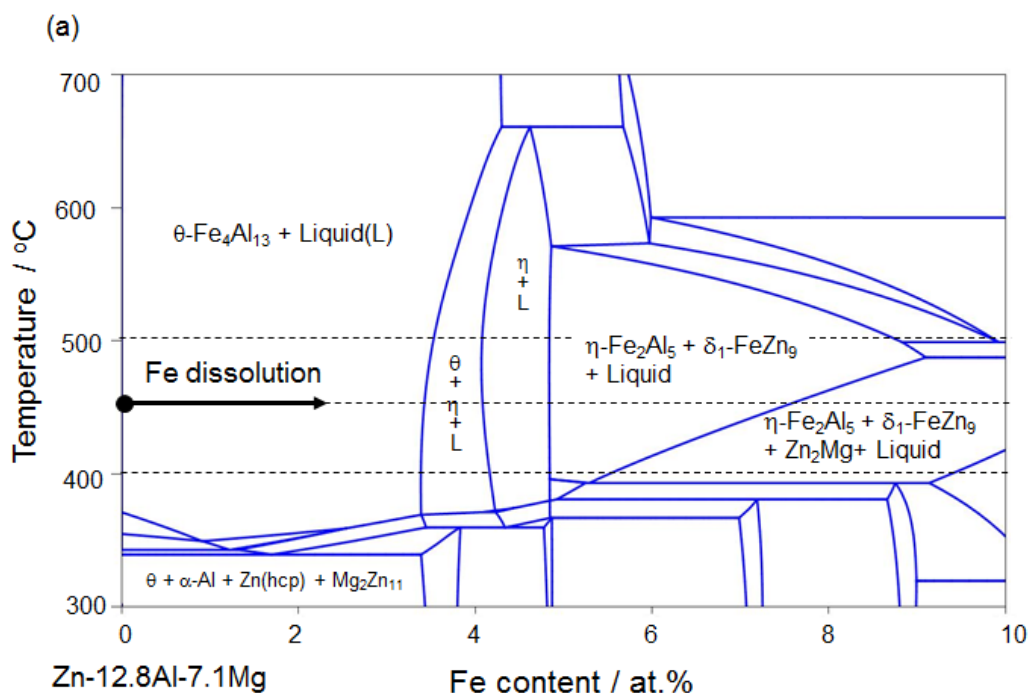


**Figure 13** (a) Calculated section of the Zn–Mg–Al–Fe quaternary phase diagram. In this section, the vertical and horizontal axes indicate the temperature and Fe content (at%), respectively. The origin on the horizontal axis corresponds to the studied alloy composition of Zn–12.8Al–7.1Mg (at%) (Zn–6Al–3Mg (wt.%)). (b–e) Schematics showing the interfacial reaction between the liquid Zn–6Al–3Mg (wt.%) and solid  $\alpha$ -Fe phases corresponding to the phase transition presented in (a).

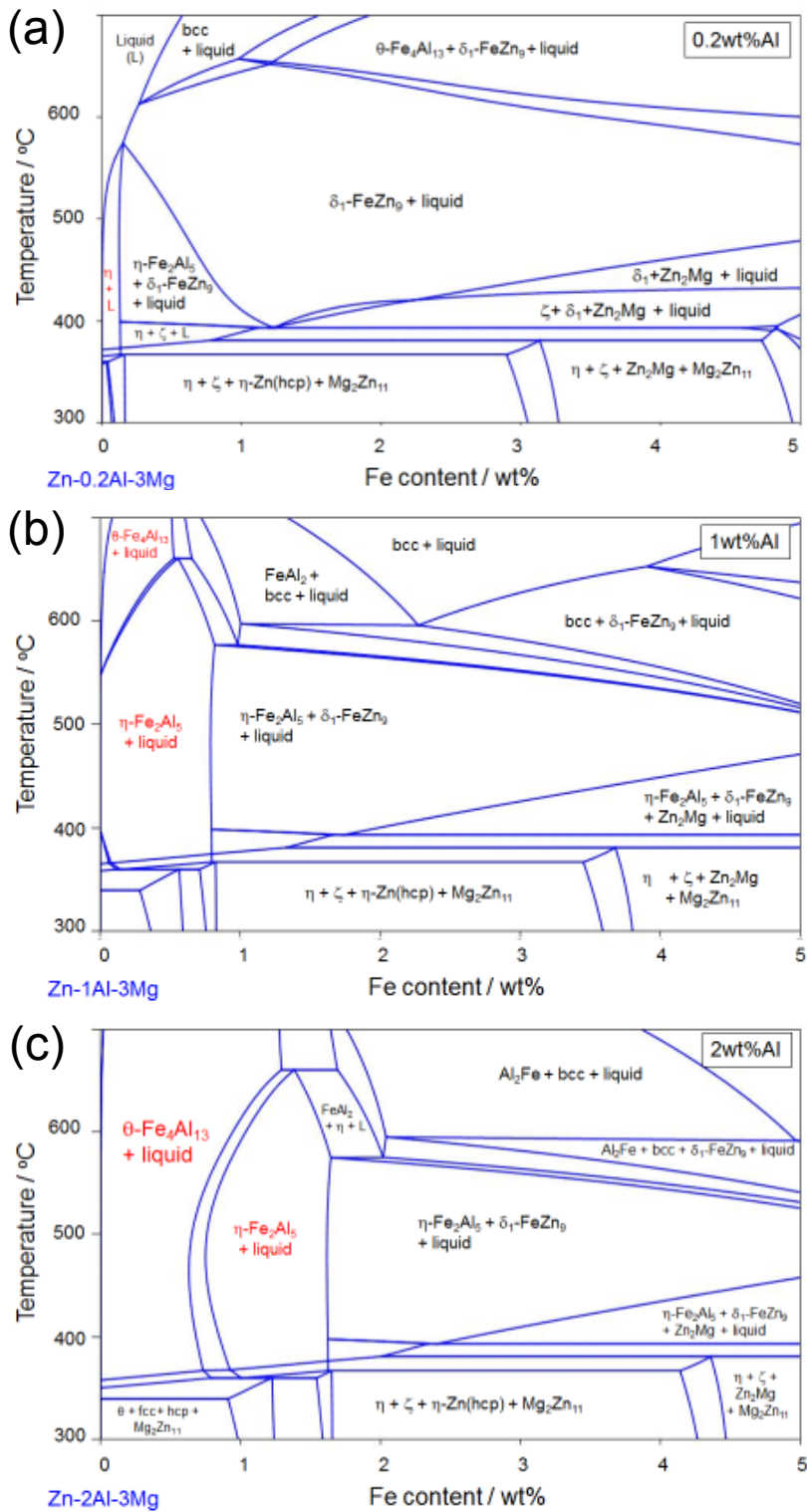


**Figure 14** Calculated sections of the Zn–Mg–Al–Fe quaternary phase diagram. In this section, the vertical and horizontal axes indicate the temperature and Fe content (wt.%), respectively. The origin on the horizontal axis corresponds to the different compositions of (a) Zn–0.2Al–3Mg, (b) Zn –1Al–3Mg and (c) Zn –2Al–3Mg (wt.%).

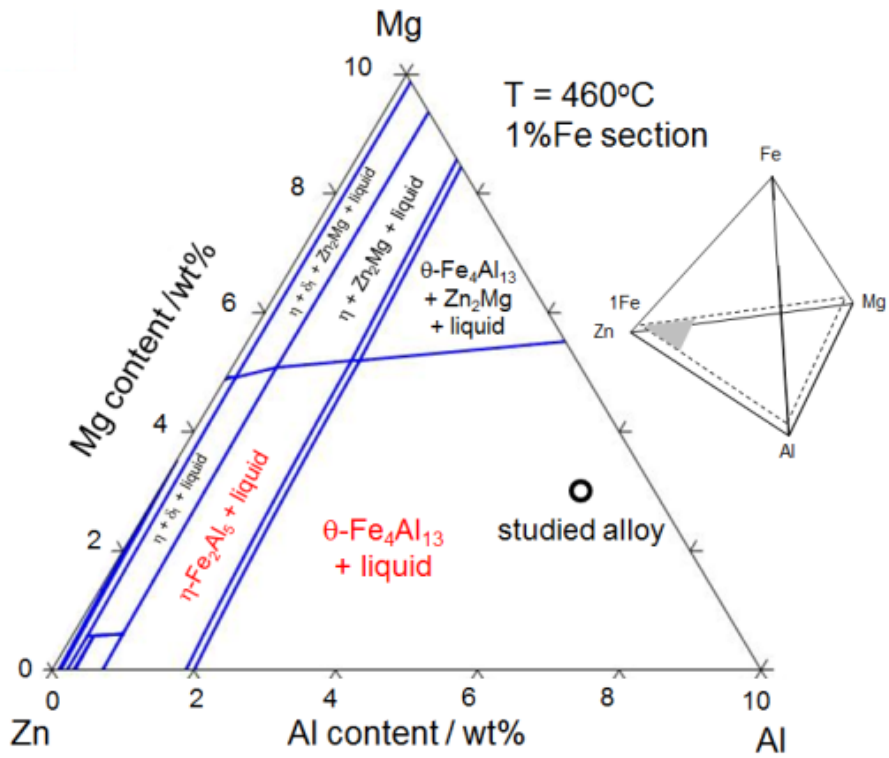


**Figure 15** Calculated section of 1 wt.% Fe at 460°C in the Zn–Mg–Al–Fe quaternary phase diagram.